Combined influence of inertia, gravity, and surface tension on the linear stability of Newtonian fiber spinning

M. Bechert*
Institute of Polymer Materials, Friedrich-Alexander-Universität Erlangen-Nürnberg, Martensstraße 7, 91058 Erlangen, Germany
and Laboratory of Fluid Mechanics and Instabilities, Ecole Polytechnique Federale de Lausanne, Lausanne 1015, Switzerland

B. Scheid
TIPs, Université Libre de Bruxelles, C.P. 165/67, 1050 Brussels, Belgium
(Received 8 March 2017; revised manuscript received 9 October 2017; published 20 November 2017)

The draw resonance effect appears in fiber spinning processes if the ratio of take-up to inlet velocity, the so-called draw ratio, exceeds a critical value and manifests itself in steady oscillations of flow velocity and fiber diameter. We study the effect of surface tension on the draw resonance behavior of Newtonian fiber spinning in the presence of inertia and gravity. Utilizing an alternative scaling makes it possible to visualize the results in stability maps of highly practical relevance. The interplay of the destabilizing effect of surface tension and the stabilizing effects of inertia and gravity lead to nonmonotonic stability behavior and local stability maxima with respect to the dimensionless fluidity and the dimensionless inlet velocity. A region of unconditional instability caused by the influence of surface tension is found in addition to the region of unconditional stability caused by inertia, which was described in previous works [M. Bechert, D. W. Schubert, and B. Scheid, Eur. J. Mech B **52**, 68 (2015); Phys. Fluids **28**, 024109 (2016)]. Due to its importance for a particular group of fiber spinning applications, a viscous–gravity–surface-tension regime, i.e., negligible effect of inertia, is analyzed separately. The mechanism underlying the destabilizing effect of surface tension is discussed and established stability criteria are tested for validity in the presence of surface tension.

DOI: 10.1103/PhysRevFluids.2.113905

I. INTRODUCTION

The process of drawing liquid threads constitutes the basis of the production of glass and polymer fibers and can be found in a multitude of variations, reaching from small-scale laboratory setups to large production plants. The general process is sketched in Fig. 1 and consists of a die of usually circular shape and a spinning wheel, which takes up the molten material extruded through the die and which is placed at a particular distance to the die. The draw ratio, i.e., the ratio of take-up to extrusion flow velocity, depicts the primary control parameter, and large values are mostly desired in order to fabricate fibers of small diameter.

The draw resonance effect is known to impose an upper limit for the draw ratio, as there exists a critical value beyond which the system becomes linearly unstable and both fiber diameter and flow velocity exhibit steady oscillations. The first theoretical attempts to calculate the critical draw ratio by means of linear stability analysis [1–3] utilized a one-dimensional and purely viscous model, i.e., neglecting the effects of inertia, gravity, and surface tension, and a critical draw ratio of about 20 was obtained. Such a model appears to be mathematically equivalent to a purely viscous film casting model of infinite width [4]. Stability analyses of extensions of these models covering inertia

*mathias.bechert@epfl.ch

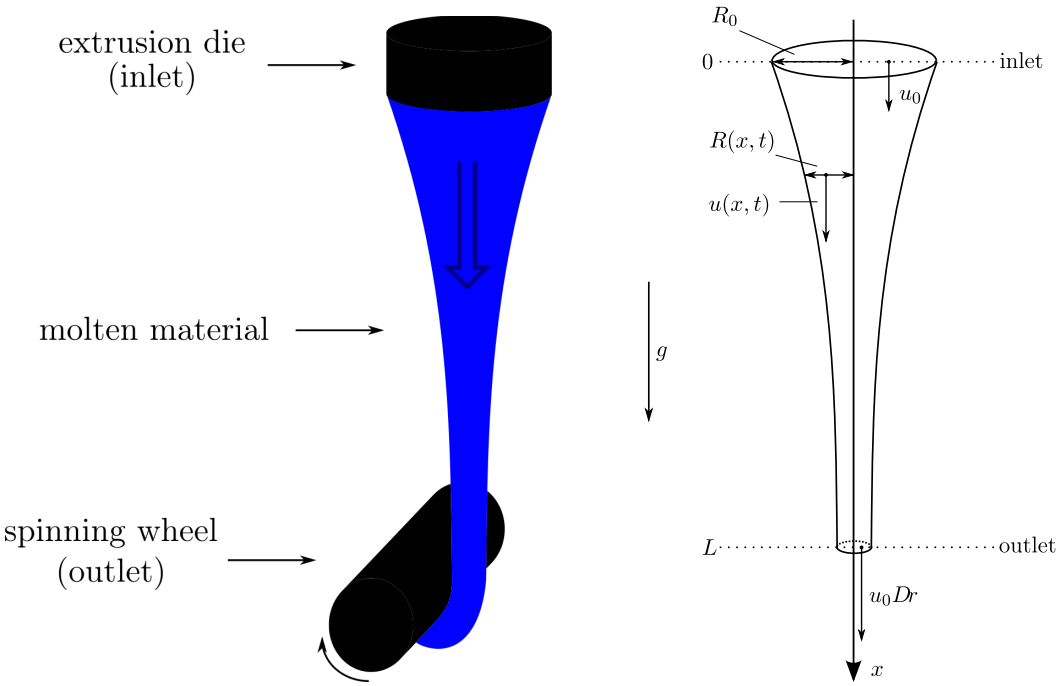

FIG. 1. Left: Sketch of the fiber spinning process. The flow direction is indicated by a big arrow and aligned with gravity. Right: Fiber model between inlet and outlet.

and gravity effects were presented and refined by various authors for fibers [5–7] and films [8,9] and the mathematical similarities between both processes remained unchanged.

In contrast to that, accounting for surface tension clearly eliminates the equivalence of the one-dimensional fiber and film models. Only a few works on the influence of surface tension on draw resonance exist. Shah and Pearson [5] investigated the effects of inertia, gravity and surface tension on isothermal and nonisothermal fiber spinning and Chang *et al.* [6] corrected the isothermal results. Both studies, however, cover the three forces separately. Another work [10] analyzed the role of surface tension in a nonisothermal scenario with varying freezing point. Both viscosity and surface energy of the material were allowed to vary with temperature, but inertia and gravity were neglected.

In most works on draw resonance in fiber spinning, surface tension is assumed to have a negligible effect. However, it can in fact be crucial for the stability behavior in some practical conditions, as will be shown in this paper by an estimation of the practical relevant parameter ranges. It has already been shown [7,9] that inertia and gravity cannot be neglected in general, and it is therefore important to investigate a model accounting for these two forces and surface tension simultaneously. The fact that the former have a stabilizing influence, while the latter is known to be destabilizing, already suggests a nontrivial extension of the surface-tension-free results. The main objective of this paper is to address this gap in the present literature.

For this purpose, a one-dimensional fiber spinning model including inertia, gravity, and surface tension forces is constructed by expanding the system of equations with respect to the aspect ratio of the fiber, following existing studies [11,12]. An alternative scaling leads to control parameters of direct practical relevance. Afterwards, the steady state and perturbation equations resulting from a linear stability analysis are derived and the neutral stability curves are tracked in the parameter space by numerical continuation. The results are discussed and visualized in stability maps and various dynamical regimes are revealed. Finally, some of the model assumptions are evaluated critically

and the stability mechanism underlying the influence of surface tension is investigated, which is followed by a review of the stability criteria proposed by Kim *et al.* [13] and Jung *et al.* [14] in the extended frame of additional surface tension effects. The paper closes with conclusions.

II. MODEL DERIVATION

A. Full model

The model used in this work concentrates on the spatial region between the extrusion die, referred to as the inlet, and the spinning wheel, referred to as the outlet. Figure 1 depicts the relevant part and the notation used for describing the state of the system. The fiber is elongated along the x axis, with the inlet at $x = 0$ and the outlet at spinning length L. The radius of the fiber is denoted by $R(x,t)$ and the velocity field by $\boldsymbol{v} = (u,v)$, with axial component u and radial component v. Fiber radius and axial velocity at the inlet are marked by index 0 and are fixed by extrusion die and speed. The outlet axial velocity u_L is fixed as well and given by $u_0\mathrm{Dr}$, with draw ratio $\mathrm{Dr} = u_L/u_0$. Note that we are assuming axial symmetry throughout this work, as the circular fiber is elongated exclusively along the vertical axis on which the inlet and outlet are located.

The following assumptions are made to derive the one-dimensional model. The material is purely Newtonian, i.e., the constitutive equation is given by

$$\boldsymbol{\sigma} = -p\boldsymbol{I} + \eta(\nabla\boldsymbol{v} + (\nabla\boldsymbol{v})^T), \tag{1}$$

with stress tensor $\boldsymbol{\sigma}$, isotropic pressure p, identity matrix $\boldsymbol{I}$, viscosity η, and differential operator $\nabla = \boldsymbol{e}_r\partial_r + \boldsymbol{e}_\varphi\partial_\varphi/r + \boldsymbol{e}_x\partial_x$, where r and φ are the radial and angular variables, respectively, and $\boldsymbol{e}_x$, $\boldsymbol{e}_r$, and $\boldsymbol{e}_\varphi$ denote the unity vectors of the cylindrical coordinate system. While derivatives of the variables with respect to φ can be neglected due to axisymmetry, the term in ∇ can still contribute to the radial components. Moreover, the slender fiber approximation, i.e., $R_0 \ll L$, applies and the material density ρ is assumed to be constant. The neglect of temperature effects and the assumption of a Newtonian material is discussed in more detail in Sec. V A 1.

The governing equations are the continuity equation,

$$\nabla\cdot\boldsymbol{v} = 0, \tag{2}$$

and the momentum conservation equation,

$$\rho(\partial_t\boldsymbol{v} + \boldsymbol{v}\cdot\nabla\boldsymbol{v}) = \nabla\cdot\boldsymbol{\sigma} + \rho\boldsymbol{g}, \tag{3}$$

with gravitational acceleration g and time variable t. Additionally, the kinematic condition and the stress boundary condition, i.e.,

$$\partial_t R + u|_R\partial_x R - v|_R = 0 \tag{4}$$

and

$$\boldsymbol{n}\cdot\boldsymbol{\sigma}|_R = \left(R_1^{-1} + R_2^{-1}\right)\gamma\boldsymbol{n}, \tag{5}$$

respectively, are valid at the fiber surface $r = R(x,t)$. Here, $\boldsymbol{n}$ denotes the vector normal to the fiber surface and is given by $\boldsymbol{n} = (-\partial_x R\,\boldsymbol{e}_x + \boldsymbol{e}_r)/\sqrt{1+(\partial_x R)^2}$, $R_1 = [1+(\partial_x R)^2]^{3/2}/\partial_{xx}R$ and $R_2 = -R\sqrt{1+(\partial_x R)^2}$ are the radii of curvature and given by basic differential geometry calculus [15], and γ denotes the material surface tension, which is assumed to be constant. The problem is closed by the following boundary conditions:

$$R(x=0) = R_0, \tag{6a}$$

$$u(x=0) = u_0, \tag{6b}$$

$$u(x=L) = u_0\mathrm{Dr}. \tag{6c}$$

Following our previous works [9,16], the system is scaled according to the following transformations:

$$x \to Lx, \quad r \to \alpha L r, \quad R \to \alpha L R, \quad u \to \sqrt{gL}\, u, \quad v \to \alpha\sqrt{gL}\, v,$$
$$t \to \sqrt{\frac{L}{g}}\, t, \quad \boldsymbol{\sigma} \to \eta\sqrt{\frac{g}{L}}\,\boldsymbol{\sigma}, \quad p \to \eta\sqrt{\frac{g}{L}}\, p, \tag{7}$$

with fiber parameter $\alpha = R_0/L$. Utilizing the free-fall velocity $\sqrt{gL}$ as a gauge originates from the assumption that the spinning length is fixed for a particular practical setup. This leads to the following dimensionless parameters:

$$Q = \frac{u_0}{\sqrt{gL}}, \quad F = \frac{\rho\sqrt{gL^3}}{\eta}, \quad \text{and} \quad S = \left(\frac{\lambda_c}{\sqrt{2R_0L}}\right)^2, \tag{8}$$

where Q and F are the dimensionless inlet velocity and fluidity,[1] respectively, whereas the dimensionless surface tension parameter S compares the capillary length $\lambda_c = \sqrt{\gamma/(\rho g)}$ with the geometric mean of the fiber dimensions. The correlations between these dimensionless parameters and the widely used Reynolds number $\mathrm{Re} = \rho\, u_0 L/\eta$, Froude number $\mathrm{Fr} = u_0^2/(gL)$, capillary number $\mathrm{Ca} = \eta\, u_0/\gamma$, and Bond number $\mathrm{Bo} = \rho g L^2/\gamma$ are straightforward and are given by

$$FQ = \mathrm{Re}, \quad \frac{F}{Q} = \frac{\mathrm{Re}}{\mathrm{Fr}}, \quad \frac{Q}{2FS} = \mathrm{Ca}^*, \quad \text{and} \quad \frac{1}{2S} = \mathrm{Bo}^*, \tag{9}$$

with rescaled Capillary and Bond numbers $\mathrm{Ca}^* = \alpha\mathrm{Ca}$ and $\mathrm{Bo}^* = \alpha\mathrm{Bo}$. The advantage of the alternative scaling is the one-to-one correlation to practical relevant parameters, assuming that the length L is fixed. Applying transformations (7), boundary conditions (6) become

$$R(x=0) = 1, \tag{10a}$$
$$u(x=0) = Q, \tag{10b}$$
$$u(x=1) = Q\mathrm{Dr}, \tag{10c}$$

while the dimensionless continuity equation (2) is merely rewritten as

$$\frac{1}{r}\partial_r(rv) + \partial_x u = 0, \tag{11}$$

and the axial and radial components of the momentum conservation equation (3) become

$$\alpha^2 F(\partial_t u + u\partial_x u + v\partial_r u - 1) = \alpha^2\partial_x\sigma_{xx} + \frac{1}{r}\partial_r(r\sigma^*_{rx}), \tag{12a}$$
$$\alpha^2 F(\partial_t v + u\partial_x v + v\partial_r v) = \frac{1}{r}\partial_r(r\sigma_{rr}) + \partial_x\sigma^*_{rx} - \frac{\sigma_{\varphi\varphi}}{r}, \tag{12b}$$

with $\sigma^*_{rx} = \alpha\sigma_{rx}$. The relevant parts of the dimensionless Newtonian constitutive equation (1) are given as

$$\sigma_{xx} = -p + 2\partial_x u, \tag{13a}$$
$$\sigma_{rr} = -p + 2\partial_r v, \tag{13b}$$
$$\sigma^*_{rx} = \partial_r u + \alpha^2\partial_x v, \tag{13c}$$
$$\sigma_{\varphi\varphi} = -p + \frac{2v}{r}, \tag{13d}$$

[1]Usually, the fluidity is merely equal to the reciprocal value of the viscosity. The present definition yields a dimensionless number based on the assumption of fixed spinning length. The term "dimensionless" is often neglected throughout this paper for the sake of convenience.

and the scaled axial and radial components of the stress boundary condition (5) read

$$\sigma_{rx}^{*}|_R - \alpha^2 \sigma_{xx}|_R \partial_x R = -2\alpha^2 F S \partial_x R \, \frac{-1 + \alpha^2[R\partial_{xx}R - (\partial_x R)^2]}{R[1 + \alpha^2(\partial_x R)^2]^{3/2}}, \tag{14a}$$

$$\sigma_{rr}|_R - \sigma_{rx}^{*}|_R \partial_x R = 2FS \frac{-1 + \alpha^2[R\partial_{xx}R - (\partial_x R)^2]}{R[1 + \alpha^2(\partial_x R)^2]^{3/2}}. \tag{14b}$$

The kinematic boundary condition (4) remains unchanged under the scaling transformation.

The slender fiber approximation enables us to expand the system variables in powers of the small parameter α, as exemplified for the axial velocity component,

$$u = u^{(0)} + \alpha^2 u^{(1)} + \mathcal{O}(\alpha^4). \tag{15}$$

With the help of Eqs. (12a) and (14a), it can be shown that

$$\sigma_{rx}^{*(0)} = \partial_r u^{(0)} = 0, \tag{16}$$

i.e., the axial velocity is independent of the radius at leading order and Eq. (11) can be integrated to give

$$v^{(0)} = -\frac{r}{2}\partial_x u^{(0)}. \tag{17}$$

The value of v at $r = 0$ was set to zero to ensure the axisymmetry assumption. Integrating the continuity equation over the scaled fiber cross section $a = \int_0^R r dr \int_0^{2\pi} \frac{d\varphi}{\pi} = R^2$ by using Eqs. (4) and (17) yields

$$\partial_t a + \partial_x (a u^{(0)}) = 0. \tag{18}$$

Due to Eqs. (13b), (14b), (16), and (17), the isotropic pressure at leading order can be written as

$$p^{(0)} = \frac{2FS}{\sqrt{a}} - \partial_x u. \tag{19}$$

Consequently, the axial component of the stress tensor at leading order becomes

$$\sigma_{xx}^{(0)} = 3\partial_x u - \frac{2FS}{\sqrt{a}}, \tag{20}$$

where the factor of 3 is the constant Trouton ratio for purely uniaxial elongation. The cross-section averaged momentum equation then results by substituting $\sigma_{rx}^{*(1)}|_R$ as obtained from the α^2 order of Eq. (14a) in the integrated α^2 order of Eq. (12a), which yields

$$Fa\left(\partial_t u^{(0)} + u^{(0)}\partial_x u^{(0)} - 1 - S\frac{\partial_x a}{a^{3/2}}\right) = \partial_x (3a\partial_x u^{(0)}). \tag{21}$$

The superscript "(0)" will be omitted from now on. It is important to note that the fluidity F scales inertia, gravity, and surface tension forces simultaneously, while the latter can be controlled independently by parameter S. The dimensionless inlet velocity Q appears only in the boundary conditions (10). For $F \to 0$, the purely viscous limit is reached. Schultz and Davis [11] state in their derivation of the one-dimensional fiber model that gravity effects can be included only for $\mathrm{Re}/\mathrm{Fr} = F/Q = \mathcal{O}(\alpha^2)$. This statement, however, arises from a different definition of the dimensionless parameters, as they use the fiber radius at inlet instead of the spinning length as characteristic length scale. The present model equations do not suffer from such a limitation of the control parameters ranges.

Table I displays realistic ranges for the practical control parameters, which were estimated based on typical values of dimensional parameters. As there exist a multitude of different fiber spinning processes, the parameter ranges are rather large and not all combinations of the single values may

TABLE I. Realistic parameter ranges for fiber spinning setups and resulting estimated ranges of the dimensionless parameters Dr, Q, F, and S (in bold).

Parameter	Definition	Range	Unit
L		$10^{-2}-1$	m
η/ρ		10^{-1}–10	$m^2\,s^{-1}$
γ/ρ		10–40	$cm^3\,s^{-2}$
u_0		10^{-3}–1	$m\,s^{-1}$
u_L		10^{-2}–10^2	$m\,s^{-1}$
R_0		10^{-1}–2	mm
α	R_0/L	10^{-4}–10^{-1}	
Dr	u_L/u_0	**5–10^5**	
Q	$u_0/\sqrt{gL}$	**10^{-4}–1**	
F	$\rho\sqrt{gL^3}/\eta$	**10^{-4}–10^2**	
S	$\gamma/(2R_0\rho gL)$	**10^{-4}–1**	

be of practical relevance. Nevertheless, the analyzed space should make it possible to use the results presented here in most contexts. Note that the lower bound for the draw ratio was arbitrarily fixed to 5, as smaller values obtained from the given ranges of inlet and outlet velocities originate from the different process types covered by the estimates and do not correspond to reasonable fiber spinning parameters.

B. Reduced models

In order to concentrate on the pure influence of surface tension on draw resonance, a reduced viscous–surface-tension model will be used. It can be obtained by neglecting the inertia and gravity terms in Eq. (21), which yields

$$-FS\frac{\partial_x a}{a^{1/2}} = \partial_x(3a\partial_x u), \tag{22}$$

while the continuity equation (18) remains unchanged. Rescaling the axial velocity[2] by Q reveals that the effective remaining control parameter is FS/Q, which is according to (9) up to a factor $1/2$ identical to the inverse of the rescaled capillary number $1/\mathrm{Ca}^*$.

Neglecting only either gravity or inertia results in a viscous–inertia–surface-tension or, respectively, a viscous–gravity–surface-tension model. While the continuity equation is unaffected by this, the momentum equation becomes for negligible gravity

$$F\,a\left(\partial_t u + u\partial_x u - S\,\frac{\partial_x a}{a^{3/2}}\right) = \partial_x(3a\partial_x u), \tag{23}$$

and for negligible inertia

$$-F\,a\left(1 + S\,\frac{\partial_x a}{a^{3/2}}\right) = \partial_x(3a\partial_x u). \tag{24}$$

These two models depend only on two effective control parameters each, which can again be seen by rescaling the axial velocity. The viscous–inertia–surface-tension model is controlled by $FQ = \mathrm{Re}$ and $FS/Q = 1/(2\,\mathrm{Ca}^*)$ and the viscous–gravity–surface-tension model by $F/Q = \mathrm{Re}/\mathrm{Fr}$ and FS/Q. These observations indicate that the scaling transformations (7) may not be the most

[2]This is equivalent to changing the velocity scale from $\sqrt{gL}$ to u_0 in (7).

appropriate choice in the case of the reduced models, as they do not directly reveal the minimum number of independent control parameters. Nevertheless, it is not possible to generally disable inertia, gravity, or surface tension in practice, but rather to tune these effects indirectly by changing the quantities corresponding to the practical control parameters Q, F, and S. Therefore, we will exclusively use these parameters within this paper in order to stick close to the practical application, but also indicate identities to other well-known dimensionless numbers to simplify comparison with existing studies.

III. STABILITY ANALYSIS

The system of equations (18) and (21) is analyzed by a linearized perturbation ansatz around the steady state, i.e.,

$$a(x,t) = a_s(x)(1 + A(x)e^{\lambda t}), \tag{25a}$$

$$u(x,t) = u_s(x)(1 + U(x)e^{\lambda t}), \tag{25b}$$

with subscript s denoting the steady state, A and U are the complex spatial perturbations, both assumed to be much smaller than unity, and $\lambda = \lambda_R + i\lambda_I$ is the complex eigenvalue. The steady state is the solution of the system of equations for $\partial_t \to 0$ and is therefore determined by the following equations:

$$a_s' = -\frac{a_s u_s'}{u_s}, \tag{26a}$$

$$u_s'' = -\frac{a_s' u_s'}{a_s} + \frac{F}{3}\left(u_s u_s' - 1 - S\frac{a_s'}{a_s^{3/2}}\right), \tag{26b}$$

where the prime denotes the derivative with respect to x. Employing Eqs. (25) in Eqs. (18) and (21) and linearizing the equations for small perturbations yield the following perturbation equations:

$$A' = -\left(\frac{\lambda}{u_s}A + U'\right), \tag{27a}$$

$$U'' = \frac{\lambda u_s'}{u_s^2}A + \frac{F}{3}\left[\left(\frac{1}{u_s} + \lambda + u_s'\right)U + u_s U' + \frac{S}{a_s^{1/2}u_s^2}\left\{\left(\lambda - \frac{u_s'}{2}\right)A - u_s' U + u_s U'\right\}\right]. \tag{27b}$$

The steady states need to fulfill boundary conditions (10) and the perturbations need to vanish at the specified positions, i.e.,

$$A(0) = U(0) = 0, \tag{28a}$$

$$U(1) = 0. \tag{28b}$$

As the eigenvalue problem (27) is linear and homogeneous, solutions can be determined with respect to one constant that fixes their amplitude. Here, we arbitrarily choose to fix the perturbation of the dimensionless force $f = 3a\partial_x u$ at the outlet to 0.1, i.e.,

$$A(1) + \frac{u_s(1)}{u_s'(1)}U'(1) = 0.1, \tag{29}$$

as this simplifies the discussion of the stability mechanism in Sec. V B.

While λ_I specifies the oscillation frequency, the sign of λ_R determines whether the system is stable ($\lambda_R < 0$) to an initial perturbation or not ($\lambda_R > 0$). The critical draw ratio Dr_c corresponds to the value of Dr at which $\lambda_R = 0$ and λ_I is equal to the frequency at criticality. These conditions define the neutral stability curves in the control parameter space spanned by Q, F, and S, which are tracked by numerical continuation utilizing the software AUTO-07P [17], as already described in

previous works [9,16,18,19]. The solution of the purely viscous limit [20,21] obtained by setting $F = 0$ and $Q = 1$ serves hereby as starting point.[3] Additionally, solution branches corresponding to extremal and constant values of the critical draw ratio are tracked in the Q-F plane for constant values of S.

In the case of the viscous–surface tension model introduced in Sec. II B, i.e., Eqs. (18) and (22), Eqs. (26b) and (27b) simplify to

$$u_s'' = -a_s'\left(\frac{u_s'}{a_s} + \frac{FS}{3a_s^{3/2}}\right), \tag{30}$$

$$U'' = \frac{\lambda u_s'}{u_s^2}A + \frac{FS}{3a_s^{1/2}u_s^2}\left[\left(\lambda - \frac{u_s'}{2}\right)A - u_s'U + u_sU'\right], \tag{31}$$

respectively, while the equations corresponding to the viscous–gravity–surface-tension model, i.e., Eqs (18) and (24), become

$$u_s'' = -\frac{a_s'u_s'}{a_s} - \frac{F}{3}\left(1 + S\frac{a_s'}{a_s^{3/2}}\right), \tag{32}$$

$$U'' = \frac{\lambda u_s'}{u_s^2}A + \frac{F}{3}\left[\frac{U}{u_s} + \frac{S}{a_s^{1/2}u_s^2}\left\{\left(\lambda - \frac{u_s'}{2}\right)A - u_s'\,U + u_s\,U'\right\}\right]. \tag{33}$$

The viscous–inertia–surface-tension model will not be analyzed in terms of linear stability, for reasons which will be given later.

IV. RESULTS

A. Isolated effect of surface tension

The neutral stability curve obtained by analyzing the viscous–surface-tension model is plotted in Fig. 2(a), as well as the data presented by Chang *et al.* [6]. The rather moderate quantitative match of both data sets and the apparent stability maximum of the latter most likely originate from the low quality of the original plot presented by Chang *et al.* [6]. Anyway, an increasing influence of surface tension has a purely destabilizing effect. For sufficiently large values of $2FS/Q$, the critical draw ratio becomes equal to or smaller than unity, which means that no stable spinning is possible beyond a threshold value of this combined control parameter; i.e., the system becomes unconditionally unstable. As visualized by Fig. 2(b), the neutral stability curve can be well fitted using the following empirical expression:

$$\mathrm{Dr}_c = (20.218 - k)e^{-p\frac{2FS}{Q}} + k, \tag{34}$$

with free parameters $p = 0.2200 \pm 0.0001$ and $k = 0.4473 \pm 0.0020$. The relative fit residual δ is shown by Fig. 2(b) and is always below 1%. Using Eq. (34), $FS/Q \geqslant 8.13$ can be calculated as critical condition for $\mathrm{Dr}_c \leqslant 1$. The numerical data yield a critical frequency $\lambda_I = 5.88$ at this point. To the best of our knowledge, this is the first time that such an unconditionally unstable region caused by the effect of surface tension is identified. The validity of the stability curve and the existence of the transition to unconditional instability in particular were additionally checked by an eigenvalue spectrum analysis using Chebyshev collocation, following the method described by Hagen and Langwallner [22], in order to ensure that the tracked instability mode from the purely viscous case remains the most unstable one for $FS/Q \neq 0$.

[3] In fact, Q and S can have arbitrary values, apart from $Q = 0$, as long as $F = 0$.

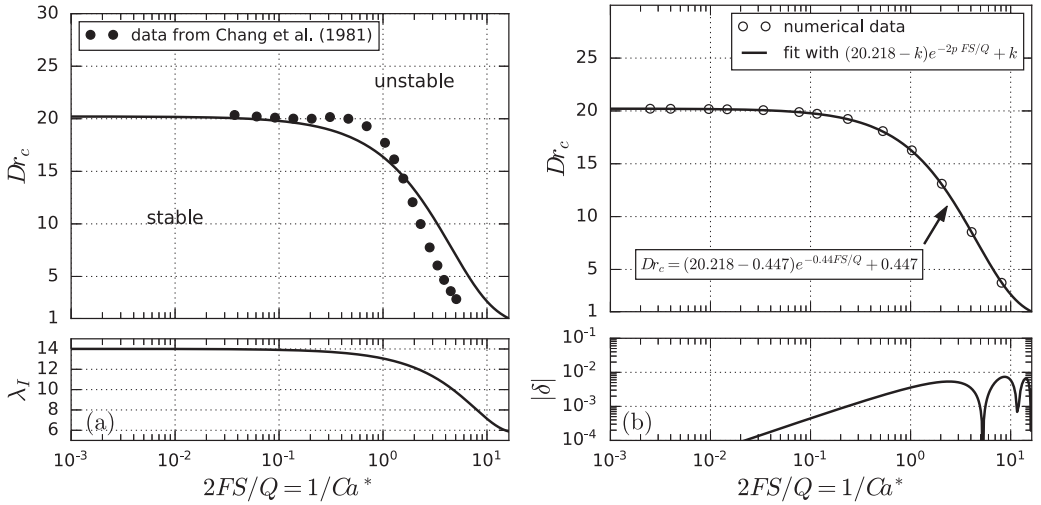

FIG. 2. (a) Top: Neutral stability curve for the viscous–surface-tension model as calculated by numerical continuation (line) together with the results of Chang *et al.* [6] (points). Bottom: Dimensionless oscillation frequency at criticality. (b) Empirical fit to the stability curve and corresponding relative fit residual $|\delta|$. Only a few points of the numerical data are shown for the sake of readability.

B. Neutral stability curves including gravity, inertia, and surface tension

Neutral stability curves for the full fiber model including gravity, inertia, and surface tension effects are depicted by Fig. 3. Figure 3(a) shows the critical draw ratio with respect to fluidity F for various combinations of dimensionless surface tension parameter S and inlet velocity Q. For $S = 10^{-3}$ and $Q = 10^{-1}$, increasing F has a purely stabilizing influence and finally leads to unconditional stability.[4] This effect is caused by inertia and was described and explained in previous studies [9,16]. For the other three curves, increasing the fluidity finally always leads to unconditional instability. For $S = 10^{-1}$ and $Q = 10^{-3}$, a monotonic destabilizing effect of increasing F can be observed, similar to increasing FS/Q for the viscous–surface-tension model. If S is reduced to $S = 10^{-3}$, a stability maximum at $F \approx 2$ appears, which is indicated by a cross. This means that, for values of the fluidity below 2, the stabilizing influence of gravity and/or inertia dominates the stability behavior, while surface tension effects lead to destabilization for larger values of F. If $S = Q = 10^{-1}$, the stability curve diverges at $F \approx 7$ and a window of unconditional stability appears. This window is limited to $F \lesssim 26$, as then the divergence changes sign and the system becomes unconditionally unstable for larger values of F. The threshold value was hereby obtained by tracking the isoline of constant $\mathrm{Dr}_c = 1$ in the Q-F plane (see next paragraph). As the influence of surface tension is tuned by FS/Q, the qualitative shape of the stability curves changes fundamentally with S and Q. The fluidity F in particular increases the effect of inertia, gravity, and surface tension simultaneously, which leads to the possible nonmonotonic behavior.

Analogous to that, stability curves with respect to Q as shown by Fig. 3(b) exhibit a large variety in qualitative shape. The curve for $S = 10^{-3}$ and $F = 10^{-2}$ has a stability minimum, and increasing low values of Q has a destabilizing influence, while increasing large values of Q stabilizes, even though this is hardly visible in the plot. If $S = 10^{-1}$ instead, increasing Q has a purely stabilizing effect over the entire domain. In the case of $F = 1$, both the region of unconditional instability for small values of Q and the region of unconditional stability for large values of Q can be observed.

[4]The term "unconditional stability" refers hereby to the linear stability behavior, i.e., with respect to infinitesimal perturbations, and does not make any statement about the finite amplitude stability.

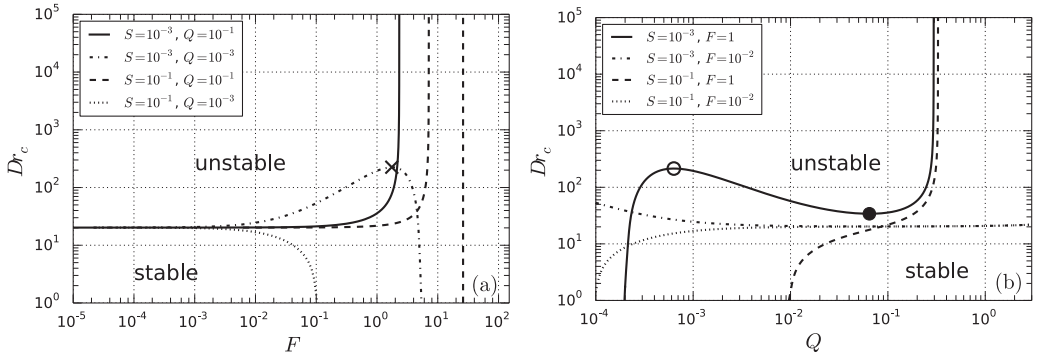

FIG. 3. Neutral stability curves for the full fiber model. (a) Critical draw ratio vs dimensionless fluidity F for various values of S and Q. (b) Critical draw ratio vs dimensionless inlet velocity Q for various values of S and F. Symbols indicate extrema, the loci of which are given in Fig. 4.

For $S = 10^{-3}$, in addition, there exist both a stability maximum at $Q \approx 6 \times 10^{-4}$, indicated by an open circle, and a stability minimum at $Q \approx 7 \times 10^{-2}$, indicated by a filled circle.

The findings above clearly demonstrate that statements about the influence of relative changes in fluidity and inlet velocity on the critical draw ratio strongly depend on the value of the dimensionless surface tension parameter S. In particular, the qualitative trend of the neutral stability curves differs fundamentally from the surface-tension-free case, which is—up to a scaling factor of the fluidity—identical to the previously studied infinite width film casting model [9].

C. Stability maps

A comprehensive overview of the stability behavior is given by the stability maps in the Q-F plane for various values of S, as shown by Fig. 4. Within these maps, solid lines indicate parameter combinations of constant critical draw ratio, with the particular values shown below the lines. A viscous region, within which Dr_c lies between 20 and 21, and deviates therefore only negligibly from the viscous value of 20.218, is shaded in light gray. The region of unconditional stability caused by inertia is shaded in dark gray, while the region of unconditional instability caused by the effect of surface tension is crossed out; the thick lines delimiting these regions correspond to the isolines of $\mathrm{Dr}_c = 10^5$, an arbitrary threshold value to unconditional stability based on the values given by Table I, and $\mathrm{Dr}_c = 1$ (unconditional instability threshold), respectively.

The surface-tension-free scenario, i.e., $S = 0$, is depicted by Fig. 4(a) and is—up to a constant factor caused by the different Trouton ratios—identical to the infinite width film casting model presented in our previous paper [9]. In this case, increasing the fluidity F has a purely stabilizing influence and finally leads to unconditional stability for all values of inlet velocity Q. A stability minimum with respect to Q for constant values of F is found, which is also illustrated by the filled circle in Fig. 3(b) and visualized by a gray, dotted line in the stability maps. The 1-to-1 slopes of the isolines reveal regions where inertia ($F \propto Q$) or gravity effects ($F \propto 1/Q$) can be neglected.

With increasing surface tension parameter S, the region of unconditional instability appears and grows, while the region of unconditional stability shrinks in the practical relevant parameter space. As already reported in the previous paragraph, increasing F can have a nonmonotonic influence on the critical draw ratio if Q is in the appropriate range. For large values of Q, all maps appear to be similar, and in fact it will be shown below that the stability is not influenced by surface tension in this parameter region. For rather small values of Q, a stability maximum with respect to F for constant values of Q appears, which is illustrated by a cross in Fig. 3(a), and the system becomes unconditionally unstable for large F. This maximum is visualized by a dashed line in the maps, which separates the parameter space into regions where increasing F has a stabilizing influence and

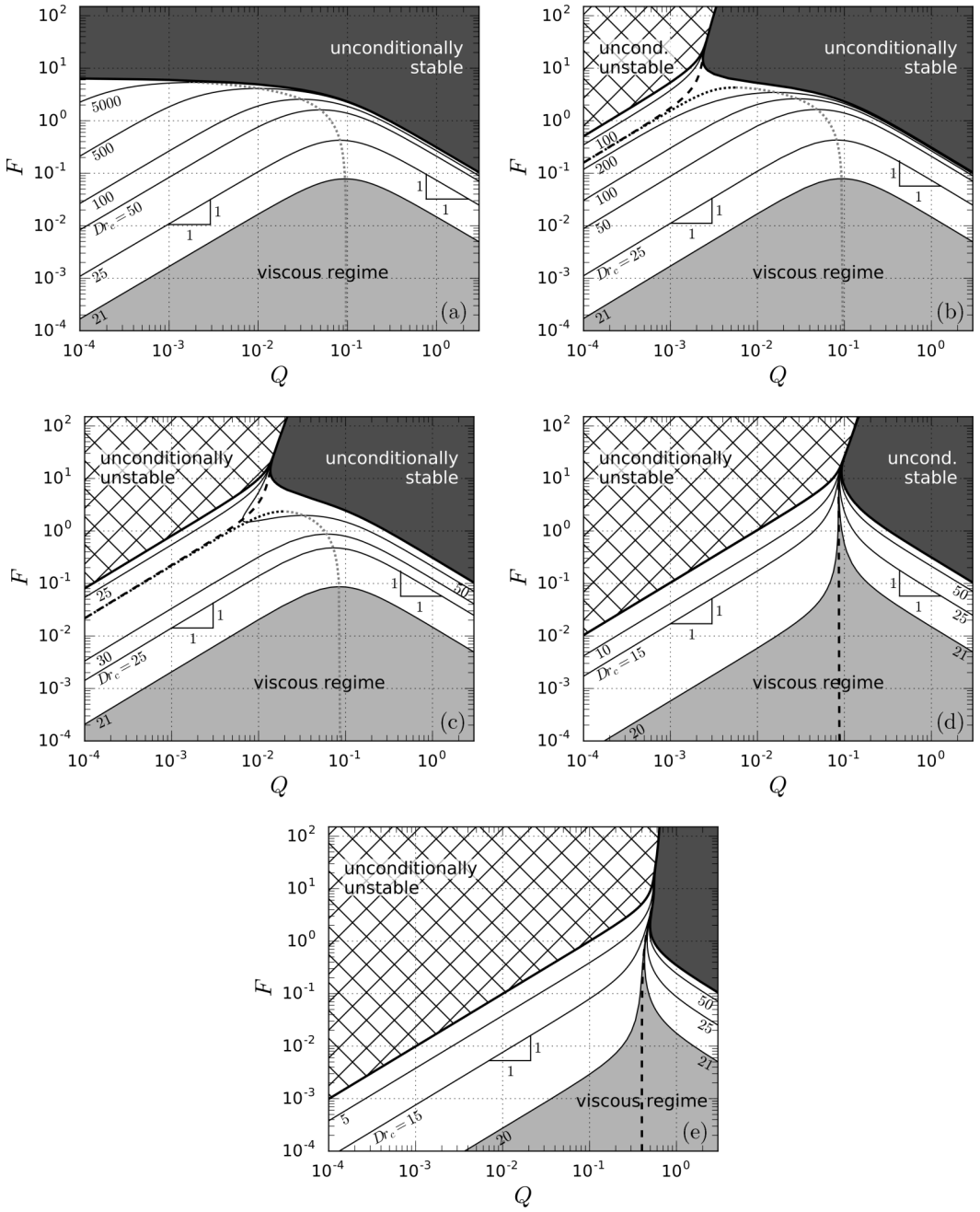

FIG. 4. Stability maps in the Q-F plane for various values of S: (a) $S = 0$, (b) $S = 10^{-3}$, (c) $S = 10^{-2}$, (d) $S = 10^{-1}$, (e) $S = 1$. Thin solid lines correspond to isolines of constant critical draw ratio, with particular values indicated below the lines. The dashed lines indicate the loci of a stability maximum with respect to F at constant Q, as illustrated by the cross in Fig. 3(a). The dotted black (gray) lines indicate the loci of a stability maximum (minimum) with respect to Q at constant F, as illustrated by the open (filled) circle in Fig. 3(b).

where it is destabilizing. For $S \gtrsim 0.1$, the maximum disappears and the separating line is parallel to the F axis; i.e., increasing F has either a purely stabilizing effect (on the right side) or a purely destabilizing effect (on the left side), depending on the value of Q being large or small, respectively.

The influence of increasing inlet velocity Q is also altered qualitatively by surface tension. The gray dotted line indicates the locus of a stability minimum with respect to Q [see filled circle in Fig. 3(b)] and connects to the black dotted line, which indicates a stability maximum [see open circle in Fig. 3(b)]. If the loci of stability maxima with respect to Q (black dotted line) and with respect to F (black dashed line) join, a local stability maximum is present and the corresponding parameter combinations are, apart from the region of unconditional stability, the most recommended for optimizing the process stability. For $S \gtrsim 0.1$, the extrema with respect to Q disappear as well, and increasing Q has a purely stabilizing effect.

The threshold lines to unconditional stability and instability, as well as all isolines of constant critical draw ratio, coincide to a common branch for large values of F. Close to this branch, a small variation in the control parameters can change the sign of the divergence of the neutral stability curves and switch from unconditional stability to unconditional instability. This shows that, especially for low-viscosity material fiber spinning, choosing the inlet velocity has a crucial effect on the overall process stability, which has been revealed through the choice of the scaling.

D. Viscous–gravity–surface-tension regime

As already mentioned above and reported in our previous work [9], viscous–gravity and viscous–inertia regimes can be deduced from the 1-to-1 slope of the isolines in the absence of surface tension. The fact that these slopes are also present for nonzero, constant values of S implies that the critical draw ratio still depends in these regions exclusively on FQ or F/Q, respectively. As pointed out in Sec. II B, the viscous–gravity–surface-tension model depends in general on F/Q and $S(F/Q)$. For constant values of S, the dynamics depend therefore solely on F/Q, in accordance with the shape of the isolines in the stability maps. On the other hand, the viscous–inertia–surface-tension model depends in general on FQ and $S(F/Q)$, which is not reducible to one control parameter for constant values of S. As the stability maps clearly show that the critical draw ratio depends only on the product of FQ, the corresponding region must belong to a pure viscous–inertia regime, where both gravity and surface tension effects can be neglected. This means that within these parameter regions the results of the surface-tension-free scenario [9] can directly be applied. As the viscous–gravity–surface-tension regions constitute a notable part of the practical parameter space, this case will be analyzed separately in the following.

Figure 5(a) shows neutral stability curves Dr_c versus F/Q for various values of S. In the absence of surface tension, i.e., $S = 0$, increasing F/Q has a purely stabilizing effect due to gravity. Otherwise, the influence of surface tension finally leads to unconditional instability above a threshold value of F/Q, which decreases with increasing S. If S is not too large, e.g., $S = 10^{-3}$–10^{-2}, a stability maximum can be observed due to the interplay of gravity and surface tension. The stability map visualized by Fig. 5(b) reveals that the stability maximum indicated by the black dashed line disappears for $S > 5.53 \times 10^{-2}$. An almost reciprocal proportionality between S and F/Q can be observed for the threshold to unconditional instability, similar to the case where gravity is neglected and the transition defined by $FS/Q \geqslant 8.13$ (see Sec. IV A), which is depicted by a thick gray line in Fig. 5(b). As the two threshold lines do not differ much, it can be stated that the transition to unconditional instability is hardly altered by gravity.

V. DISCUSSION

A. Evaluation of model assumptions

1. Newtonian fluid and isothermal conditions

Among the various model assumptions mentioned in Sec. II, the neglect of viscoelastic and temperature effects may appear to be rather strongly limiting. The main reason why these assumptions

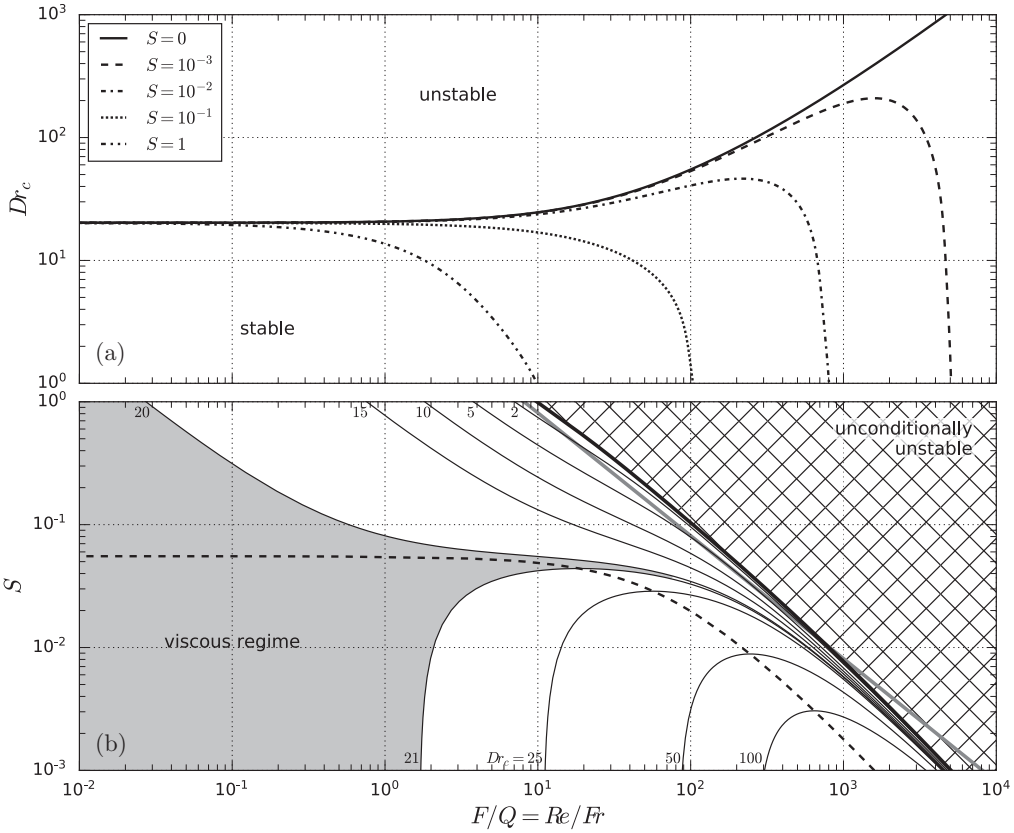

FIG. 5. Stability behavior in the viscous–gravity–surface-tension regime. (a) Neutral stability curves Dr_c vs F/Q for various values of S. (b) Stability map with isolines of constant critical draw ratio, with particular values indicated on the left of the lines. The thick black line visualizes the transition to unconditional instability, i.e., $\mathrm{Dr}_c \leqslant 1$. The thick gray line corresponds to the transition to unconditional instability of the viscous–surface-tension model, neglecting gravity, as discussed in Sec. IV A. The dashed line indicates the loci of a stability maximum with respect to F/Q at constant S and separates the parameter space into regions where increasing F/Q is purely stabilizing (below) and purely destabilizing (above).

are made is that respecting the influence of viscoelasticity or temperature variation each implies at least one or two additional control parameters, which would go beyond the scope of the present analysis. Nevertheless, assuming an isothermal process with a Newtonian fluid is still practically relevant. Besides polymer melts, molten glass is often used in fiber spinning processes and is known to behave like a Newtonian fluid. But also polymer melts do not necessarily show viscoelastic behavior. Depending on the particular processing conditions and the relaxation time(s) of the material, the viscosity of a polymer melt can be constant in good approximation during the whole process ("Newtonian plateau") and elastic effects are generally negligible if the dominant relaxation time of the material is sufficiently small compared to the fluid propagation time, i.e., the Deborah number being small. In general, it is known that viscoelastic effects can have a significant influence. Studies employing the upper-convected Maxwell or White-Metzner models [23,24] show a stabilizing influence of increasing viscoelastic effects. In contrast to that, and probably due to the strong strain hardening prediction of the upper-convected Maxwell model, more realistic viscoelastic models show a primarily destabilizing effect of viscoelasticity [25,26]. The way viscoelastic effects interact with the presented effects of inertia, gravity, and surface tension is still an open and interesting question. In

the case of film casting of poylmer solutions, German and Khayat [27] have analyzed the combined influence of inertia and elasticity on draw resonance employing a Phan-Thien–Tanner model.

It is well known that cooling can have a highly stabilizing effect on the draw resonance instability [28,29]. In many industrial processes, a particular cooling profile is applied along the spinline for this reason. On the other hand, temperature effects may be rather moderate or even negligible if the material is cooled exclusively by the ambient air. In its simplest form, the change in temperature is tuned by the Stanton number [28], which depends on both material properties like the heat conductivity and process parameters like the flow speed and the fiber radius. More precisely, large flow velocity, fiber radius and heat capacity, and small heat conductivity and spinning length all reduce the effect of cooling on the spinning dynamics. For example, spinning of a common polypropylene with a spinning length of 10 cm, a fiber radius of the order of 1 mm, and an axial flow speed of the order of 10^{-2} m s^{-1} already leads to a Stanton number of the order of 10^{-3}, and therefore temperature effects play at most a minor role in this case.

In conclusion, it can be stated that while assuming isothermal conditions and a Newtonian fluid can be justified and is reasonable for several experimental setups, it has to be kept in mind that the transition to draw resonance may be altered for typical industrial processes by the effects of viscoelasticity and cooling. Especially the latter may lead to additional regions of high stability in the parameter space. Apart from that, it was shown in our previous works [9,16] as well as in the present one that the effect of inertia can lead to very high or even unconditional stability, which is also a possible explanation for the sometimes discussed discrepancy between the purely viscous value of $\mathrm{Dr}_c \approx 20$ and typical (stable) draw ratios in industrial processes, which can be several orders of magnitude higher (see Table I). Other effects which are also assumed to have a stabilizing influence are the freezing of the fiber due to cooling [10,30] and different take-up conditions, e.g., using blown air instead of a spinning wheel, as it has been shown that different boundary conditions at the outlet may change the stability behavior significantly. [20,21]

2. *Neglect of the streamwise curvature*

The derivation of the leading order equations in Sec. II A includes neglecting the streamwise curvature, as Eqs. (14) reveal that the corresponding terms are of $\mathcal{O}(\alpha^2)$. Nevertheless, this step has to be analyzed carefully, as the terms scale as well with the product of the control parameters F and S. By tuning the control parameters far from unity, the influence of the streamwise curvature may thus become significant, analogous to the well-known Rayleigh-Plateau instability, where it has a stabilizing influence for large wave numbers [31]. In the following, we will demonstrate that this issue is not relevant for the present results, especially with respect to the detected threshold to unconditional instability.

First, it has to be noted that the right-hand side of Eqs. (14) scales in fact with $2FS/Q$, which is identical to $1/\mathrm{Ca}^*$ according to (9), but the influence of Q is hidden in the boundary conditions (10), which becomes clearer if the velocity is scaled by u_0 instead of $\sqrt{gL}$. As a consequence, the streamwise curvature has negligible influence at leading order as long as

$$1/\mathrm{Ca}^* = \frac{2FS}{Q} \ll \alpha^{-2}. \tag{35}$$

Figure 2 shows that the transition to unconditional instability occurs in the absence of inertia and gravity effects at $1/\mathrm{Ca}^* \approx 16$, which is in any case much smaller than α^{-2} according to Table I, and therefore the transition is not generally suppressed by the stabilizing influence of the streamwise curvature. The ranges of Q, F, S, and α as given in Table I may suggest that criterion (35) is not always fulfilled in the entire parameter space presented by the stability maps in Fig. 4. These cases, however, correspond to rather irrelevant scenarios for practical application. Materials with large fluidity, for instance, are mostly processed with long spinning lengths and small radii, which ensures that condition (35) is usually fulfilled and the streamwise curvature term can safely be neglected. Nevertheless, we advice to check the condition separately for each process prior to applying the present model and results.

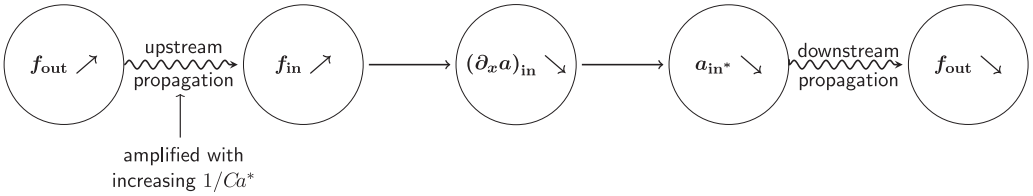

FIG. 6. Visualization of one half period of draw resonance. The wavy arrows indicate propagation along the spinline. The indices indicate the positions at inlet and outlet, in* denotes a position close to the inlet.

B. Comments on the stability mechanism

In order to investigate the destabilizing mechanism underlying the effect of surface tension on draw resonance, the viscous–surface-tension model as introduced in Sec. II B will be used, which means that the only remaining control parameter is $1/\mathrm{Ca}^* = 2FS/Q$.

As pointed out by Kim *et al.* [13] and reconsidered recently [16,18], draw resonance can be understood in terms of flow perturbation waves traveling along the spinline. The flow perturbations at the inlet are caused by force perturbations at the outlet traveling towards the inlet, with the force given by $f = 3a\partial_x u$. This can be seen by rewriting continuity equation (18) as

$$(\partial_x a)_{\text{in}} = -\frac{f_{\text{in}}}{3}, \tag{36}$$

where the boundary conditions were applied to set $(\partial_t a)_{\text{in}} = 0$ and $u_{\text{in}} = 1$. The indices indicate the positions at *in*let and *out*let. The diagram in Fig. 6 describes one half period of draw resonance, starting with a temporal increase of the force at the outlet, which afterwards is propagating upstream towards the inlet. At the inlet, it leads according to Eq. (36) to a decrease of the (negative) gradient of the cross section, which means that the cross section close to the inlet (indicated by an asterisk) decreases. This reduced cross section then travels downstream until it approaches the outlet, where it leads to a reduction of the force. The second half period of draw resonance corresponds to the same diagram with all oblique arrows inverted.

In the purely viscous limit, i.e., neglecting inertia, gravity, and surface tension, the momentum equation yields a force independent of the axial position, i.e., instantaneous propagation of the force perturbations from outlet to inlet, and a uniform perturbation amplitude. Secondary forces alter the wave propagation, however. In a previous study [16], the stabilizing effect of inertia and gravity could be correlated to a reduction of the force oscillation amplitudes towards the inlet, which means that the feedback loop of draw resonance is damped.

Figures 7(a)–7(c) depict the time evolution of force perturbation waves along the spinline for the viscous–surface-tension fiber spinning model for three values of $1/\mathrm{Ca}^* = 0.1$, 5, and 10. As prescribed by boundary condition (29), both the amplitude and phase of the force perturbation at the outlet are fixed. For the two larger values of the control parameter, it can be observed that the influence of surface tension leads to an increase of the oscillation amplitude at the inlet as compared to the outlet. The ratio of force perturbation amplitudes at inlet to outlet is plotted in Fig. 7(d) with respect to $1/\mathrm{Ca}^*$. With increasing influence of surface tension, the amplification of the perturbation towards the inlet becomes stronger if $1/\mathrm{Ca}^*$ is not too large. This can also be understood in light of the Rayleigh-Plateau instability mechanism, as the radially acting capillary force tends to amplify perturbations in the fiber. With increasing fiber radius towards the inlet, the counteracting capillary pressure decreases according to Eq. (19) and becomes minimum at the inlet.

There exists, however, a maximum of the amplitude ratio at $1/\mathrm{Ca}^* \approx 9$, which is near the inflection point visible in Fig. 2(a). For larger values of $1/\mathrm{Ca}^*$, the perturbation amplitude ratio decreases while the critical draw ratio also decreases. There exist at least two possible explanations for this apparent contradiction. First, the additional phase variation of the force perturbations along the spinline, which becomes clearly visible in Fig. 7(c) for $1/\mathrm{Ca}^* = 10$, can influence the propagation

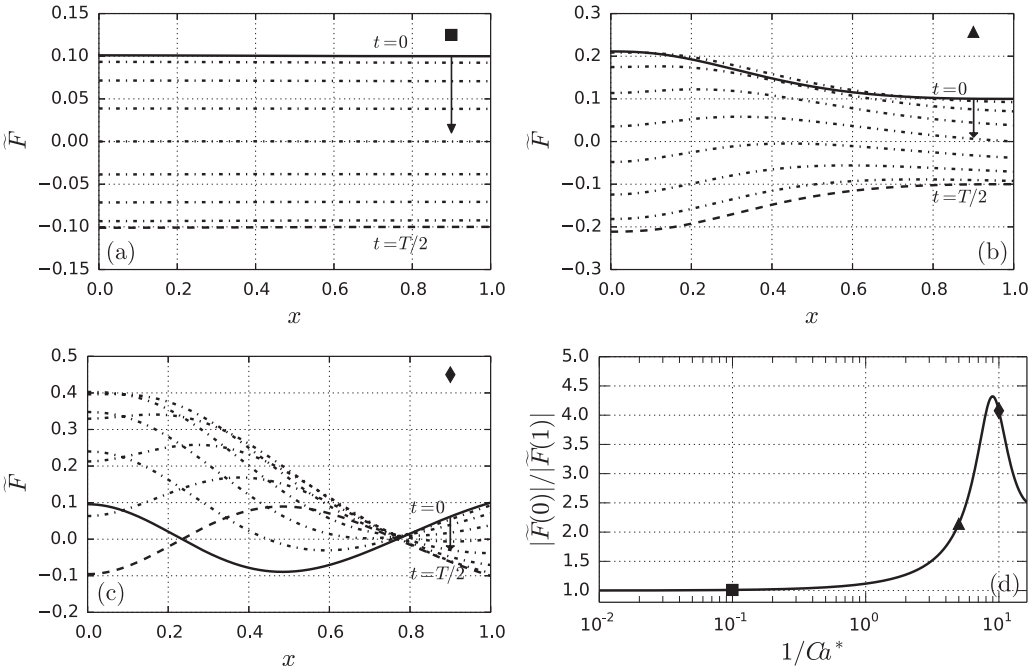

FIG. 7. Evolution of the force perturbation waves in space and time. Plots (a), (b), and (c) visualize the force perturbation $\widetilde{F} = f/f_s - 1$ along the x axis at various time values within a half oscillation period $T/2$ for $1/\mathrm{Ca}^* = 0.1$ (a), 5 (b), and 10 (c), respectively. Time evolves from the thick line ($t = 0$) to the dashed line ($t = T/2$) along the arrow in steps of $T/16$, with each step shown by a dashed-dotted line. (d) Ratio of oscillation amplitudes of force perturbation $\widetilde{F}$ at inlet to outlet.

of the force perturbation waves. While for smaller values of $1/\mathrm{Ca}^*$ the destabilization is then mostly caused by the amplification of the oscillation amplitude, the modification of the perturbation phase becomes more important for larger values of $1/\mathrm{Ca}^*$ and leads to further destabilization even though the amplitude ratio decreases. Second, the instability mechanism of the formerly mentioned Rayleigh-Plateau instability can become dominant for large values of $1/\mathrm{Ca}^*$ and therefore governs the stability behavior. To investigate this issue further, a systematic treatment of the dynamics of the perturbation waves is needed, which, however, goes beyond the scope of this paper.

C. Validity of alternative stability criteria

Based on the picture of traveling perturbation waves along the spinline, Kim *et al.* [13] derived a stability criterion for the onset of draw resonance for a purely viscous model. At critical conditions, it can be written as

$$t_L + T/4 = \theta_L, \tag{37}$$

with traveling time of a unity-throughput wave t_L, oscillation period T, and maximum- or minimum-cross-section wave traveling time θ_L. The criterion was already verified for additional inertia and gravity effects [16]. Figure 8(a) shows each term of Eq. (37) at criticality in dependence of $1/\mathrm{Ca}^*$. The unity-throughput wave traveling time is calculated analogously to the previously derived equations for film casting [16,18] by

$$t_L = \int_0^1 \frac{dx}{u_s} \frac{A_R(A_R + U_R) + A_I(A_I + U_I)}{(A_R + U_R)^2 + (A_I + U_I)^2}, \tag{38}$$

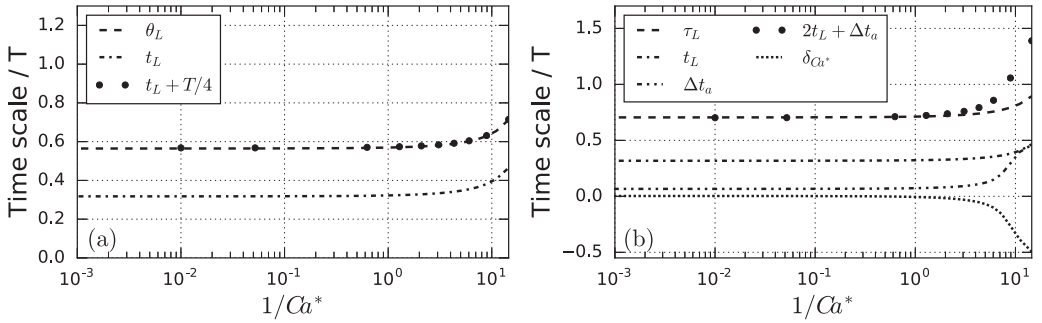

FIG. 8. Check of (a) the stability criterion proposed by Kim *et al.* [13] and (b) the approximation from Jung *et al.* [14] at criticality. The time is scaled by the oscillation period T and only a few points are shown for $t_L + T/4$ and $2t_L + \Delta t_a$ for the sake of readability.

with indices R and I denoting the real and imaginary parts, respectively. θ_L was determined by tracking a maximum cross-section perturbation at criticality from inlet to outlet. The oscillation period T can directly be gained from the imaginary part of the complex eigenvalue λ. The plot shows perfect coincidence between the two sides of Eq. (37) and therefore indicates the validity of Kim's stability criterion in the presence of surface tension. This also confirms once again the universality of the traveling perturbation wave approach.

Jung *et al.* [14] proposed an approximation to Kim's criterion, which reads in the case of unstable conditions

$$2t_L + \Delta t_a \leqslant \tau_L, \tag{39}$$

with the equality holding at criticality. Δt_a denotes the oscillation phase difference between cross-section and force perturbation waves at the outlet, which is equal to the complex angle of $A(1)$, as the phase of the force at the outlet is kept fixed at zero according to condition (29). τ_L is the fluid residence time defined as $\tau_L = \int_0^1 dx u_s^{-1}$. While Jung's approximative criterion could be verified for a viscous–gravity model, it failed to cover inertia effects, where an additional, *a priori* unknown phase needs to be added to Eq. (39) [16]. The validation of the criterion in the presence of surface tension is checked using the plot in Fig. 8(b). While the two sides of Eq. (39) coincide for small values of $1/\mathrm{Ca}^*$, they clearly mismatch for $1/\mathrm{Ca}^* > 3$. In this case, an additional phase δ_{Ca^*} would be needed on the left-hand side of Eq. (39). The effect of surface tension leads to a phase difference Δt_a of up to $T/2$, which means that force and cross-section oscillations are almost in phase opposition at the outlet. The strong variation of the oscillation phase along the spinline for large values of $1/\mathrm{Ca}^*$ was already shown by Fig. 7(c) and it is assumed that Jung's approximation does not hold under these circumstances.

VI. CONCLUSIONS

Within the present study, the effects of inertia, gravity, and surface tension on draw resonance in Newtonian fiber spinning were investigated for the first time simultaneously. Cross-section-averaged, one-dimensional model equations were derived by expansion in a small fiber parameter and an alternative scaling yielded the fluidity, the inlet velocity and a surface tension parameter as dimensionless control parameters with direct correlation to practical application. Practical relevant ranges of these control parameters were estimated and revealed that surface tension cannot generally be neglected in the description of fiber spinning, albeit this is mostly disregarded in literature.

Utilizing a linear stability analysis, the influence of surface tension on the critical draw ratio was first examined in isolation without accounting for inertia and gravity. Previous results [6] were corrected quantitatively and a novel empirical stability criterion of high accuracy was proposed. Moreover, a region of unconditional instability was revealed, where the critical draw ratio is equal to

or below unity. In the additional presence of inertia and gravity, neutral stability curves with respect to fluidity and inlet velocity were calculated, and they exhibit a strong sensitivity on the value of the surface tension parameter and possible nonmonotonic stability behavior.

The stability maps developed in previous works [9,16] were extended to cover the effect of surface tension. The regions of unconditional stability and instability appear to lie next to each other, leading to a crucial dependence of the overall stability on the inlet velocity. Local stability maxima with respect to both fluidity and inlet velocity caused by the interplay of the destabilizing effect of surface tension and the stabilizing effects of inertia and gravity were tracked in the parameter space. Apart from the purely viscous and the unconditionally stable and unstable regions, a viscous–gravity–surface-tension regime and a viscous–inertia regime turned out to be the most relevant in the practical parameter range. The former was analyzed separately and the transition to unconditional instability turned out to be hardly influenced by gravity. The possibility to determine the relevant effects influencing the critical draw ratio in dependence on the practical parameter ranges by the shape of the isolines make the stability maps an efficient tool to choose appropriate model assumptions for a particular setup.

While the chosen model assumptions can be justified with respect to typical practical applications, one has to be generally aware that there exist conditions within which viscoelastic or temperature effects influence the stability additionally. The destabilizing effect of surface tension can mainly be explained by the traveling wave approach, with force perturbations being amplified towards the inlet. A systematic treatment of the perturbation wave dynamics, which should also shed light on the role of the Plateau-Rayleigh instability while taking into account the streamwise curvature, is still missing. Finally, the stability criterion proposed by Kim *et al.* [13] could successfully be extended to cover surface tension effects, while the approximative criterion of Jung *et al.* [14] fails at criticality if the influence of surface tension is too strong, typically $1/\mathrm{Ca}^* > 1$.

ACKNOWLEDGMENTS

The authors thank François Gallaire for fruitful discussions during the revision process. M.B. thanks Dirk Schubert and B.S. thanks the Fonds De La Recherche Scientifique - FNRS and the IAP-7/38 MicroMAST project for supporting this research.

[1] J. R. A. Pearson and M. A. Matovich, Spinning a molten threadline. Stability, Ind. Eng. Chem. Fundam. **8**, 605 (1969).
[2] D. Gelder, The stability of fiber drawing processes, Ind. Eng. Chem. Fundam. **10**, 534 (1971).
[3] S. Kase, Studies on melt spinning. IV. On the stability of melt spinning, J. Appl. Polym. Sci. **18**, 3279 (1974).
[4] Y. L. Yeow, On the stability of extending films: A model for the film casting process, J. Fluid Mech. **66**, 613 (1974).
[5] Y. T. Shah and J. R. A. Pearson, On the stability of nonisothermal fiber spinning-general case, Ind. Eng. Chem. Fundam. **11**, 150 (1972).
[6] J. C. Chang, M. M. Denn, and F. T. Geyling, Effects of inertia, surface tension, and gravity on the stability of isothermal drawing of Newtonian fluids, Ind. Eng. Chem. Fundam. **20**, 147 (1981).
[7] R. German, R. E. Khayat, and J. K. Cui, Influence of inertia and gravity on the stability of filament jet flow, Phys. Fluids **18**, 064108 (2006).
[8] F. Cao, R. E. Khayat, and J. E. Puskas, Effect of inertia and gravity on the draw resonance in high-speed film casting of Newtonian fluids, Int. J. Solids Struct. **42**, 5734 (2005).
[9] M. Bechert, D. W. Schubert, and B. Scheid, Practical mapping of the draw resonance instability in film casting of Newtonian fluids, Eur. J. Mech B **52**, 68 (2015).

[10] T. Hagen, On the effects of spinline cooling and surface tension in fiber spinning, Z. Angew. Math. Mech. **82**, 545 (2002).
[11] W. W. Schultz and S. H. Davis, One-dimensional liquid fibers, J. Rheol. **26**, 331 (1982).
[12] J. Dewynne, J. R. Ockendon, and P. Wilmott, On a mathematical model for fiber tapering, SIAM J. Appl. Math. **49**, 983 (1989).
[13] B. M. Kim, J. C. Hyun, J. S. Oh, and S. J. Lee, Kinematic waves in the isothermal melt spinning of Newtonian fluids, AIChE J. **42**, 3164 (1996).
[14] H. W. Jung, H.-S. Song, and J. C. Hyun, Draw resonance and kinematic waves in viscoelastic isothermal spinning, AIChE J. **46**, 2106 (2000).
[15] J. A. Dantzig and C. L. Tucker, *Modeling in Materials Processing* (Cambridge University Press, Cambridge, 2001).
[16] M. Bechert, D. W. Schubert, and B. Scheid, On the stabilizing effects of neck-in, gravity, and inertia in Newtonian film casting, Phys. Fluids **28**, 024109 (2016).
[17] E. Doedel, A. Champneys, T. Fairgrieve, Y. Kuznetsov, B. Sandstede, and X. Wang, AUTO97 continuation and bifurcation software for ordinary differential equations,1997; AUTO software is freely distributed on http://indy.cs.concordia.ca/auto/.
[18] B. Scheid, S. Quiligotti, B. Tran, R. Gy, and H. A. Stone, On the (de)stabilization of draw resonance due to cooling, J. Fluid Mech. **636**, 155 (2009).
[19] B. Scheid, S. Quiligotti, B. Tran, and H. A. Stone, Lateral shaping and stability of a stretching viscous sheet, Eur. Phys. J. B **68**, 487 (2009).
[20] W. W. Schultz and S. H. Davis, Effects of boundary conditions on the stability of slender viscous fibers, J. Appl. Mech. **51**, 1 (1984).
[21] M. Renardy, Draw resonance revisited, SIAM J. Appl. Math. **66**, 1261 (2006).
[22] T. Hagen and B. Langwallner, A numerical study on the suppression of draw resonance by inertia, Z. Angew. Math. Mech. **86**, 63 (2006).
[23] R. J. Fisher and M. M. Denn, A theory of isothermal melt spinning and draw resonance, AIChE J. **22**, 236 (1976).
[24] D. Silagy, Y. Demay, and J.-F. Agassant, Study of the stability of the film casting process, Polym. Eng. Sci. **36**, 2614 (1996).
[25] V. R. Iyengar and A. Co, Film casting of a modified Giesekus fluid: Stability analysis, Chem. Eng. Sci. **51**, 1417 (1996).
[26] K. Gupta and P. Chokshi, Weakly nonlinear stability analysis of polymer fibre spinning, J. Fluid Mech. **776**, 268 (2015).
[27] R. German and R. E. Khayat, Interplay between inertia and elasticity in film casting, J. Fluids Eng. **130**, 081501 (2008).
[28] Y. T. Shah and J. R. A. Pearson, On the stability of nonisothermal fiber spinning, Ind. Eng. Chem. Fundam. **11**, 145 (1972).
[29] G. K. Gupta, W. W. Schultz, E. M. Arruda, and X. Lu, Nonisothermal model of glass fiber drawing stability, Rheol. Acta **35**, 584 (1996).
[30] J. R. A. Pearson, Y. T. Shah, and R. D. Mhaskar, On the stability of fiber spinning of freezing fluids, Ind. Eng. Chem. Fundam. **15**, 31 (1976).
[31] F. Charru, *Hydrodynamic Instabilities* (Cambridge University Press, Cambridge, 2011).